Supplementary information

Low-Valence Titanium Oxides Synthesized by Electric Field Control as Novel Conversion Anodes for High Performance Sodium-Ion Batteries

Hongwei Tao†, Ruxing Wang†, Yun Tang, Min Zhou, Kangli Wang, Jianwei Hu, Pingyuan Feng, Manlin Chen, Haomiao Li and Kai Jiang**

State Key Laboratory of Advanced Electromagnetic Engineering and Technology, School of Electrical and Electronic Engineering, Huazhong University of Science and Technology, Wuhan, Hubei 430074, China

E-mail: kjiang@hust.edu.cn (K. Jiang), minzhou0729@hust.edu.cn (M. Zhou)

† These authors contributed equally to this work

Theoretical calculations

The Vienna Ab Initio Package (VASP)[1,2] was employed to perform all the density functional theory (DFT) calculations within the generalized gradient approximation (GGA) using the PBE[3] formulation. The projected augmented wave (PAW) potentials[4,5] was chosen to describe the ionic cores and the valence electrons were taken into account using a plane wave basis set with a kinetic energy cutoff of 450 eV. Partial occupancies of the Kohn-Sham orbitals were allowed using the Gaussian smearing method and a width of 0.05 eV. The on-site corrections (DFT+U) have been applied to the 3d electron of Ti atoms (Ueff=4.2 eV) by the approach from Dudarev et al.[6] The electronic energy was considered self-consistent when the energy change was smaller than 10^{-5} eV. A geometry optimization was considered convergent when the force change was smaller than 0.02 eV/Å.

The equilibrium lattice constants of hexagonal Ti_2O unit cell were optimized, when using a 15×15×9 Monkhorst-Pack k-point grid for Brillouin zone sampling, to be a=b=3.0094 and c=4.9203 Å. The unit cell was used to construct a Ti_2O supercell with 3×3×2 periodicity in the x, y and z directions, respectively. This supercell contains 36 Ti and 18 O atoms. During structural optimizations, a 4×4×3 k-point grid in the Brillouin zone was used for k-point sampling, and all atoms were allowed to relax.

The equilibrium lattice constant of NaCl-type TiO unit cell was optimized, when using a 9×9×9 Monkhorst-Pack k-point grid for Brillouin zone sampling, to be a=4.3469 Å. The unit cell was used to

construct a TiO supercell with 2×2×2 periodicity in the x, y and z directions, respectively. This supercell contains 32 Ti and 32 O atoms. During structural optimizations, a 4×4×4 k-point grid in the Brillouin zone was used for k-point sampling, and all atoms were allowed to relax.

The equilibrium lattice constants of tegragonal anatase-TiO_2 unit cell were optimized, when using a 10×10×4 Monkhorst-Pack k-point grid for Brillouin zone sampling, to be a=b=3.8498 and c=9.6627 Å. The unit cell was used to construct a TiO_2 supercell with 2×2×1 periodicity in the x, y and z directions, respectively. This supercell contains 16 Ti and 32 O atoms. During structural optimizations, a 5×5×4 k-point grid in the Brillouin zone was used for k-point sampling, and all atoms were allowed to relax.

1. The photo images of raw TiO_2, TiO and Ti_2O.

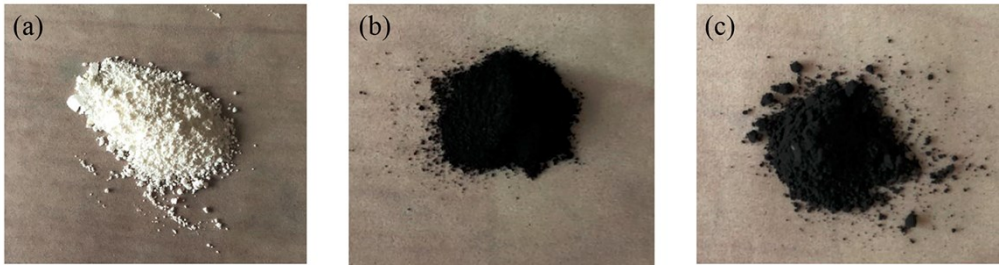

Figure S1 The photo images of (a) raw TiO_2, (b) TiO and (c) Ti_2O

2. Rietveld refined XRD patterns of raw TiO_2, TiO and Ti_2O.

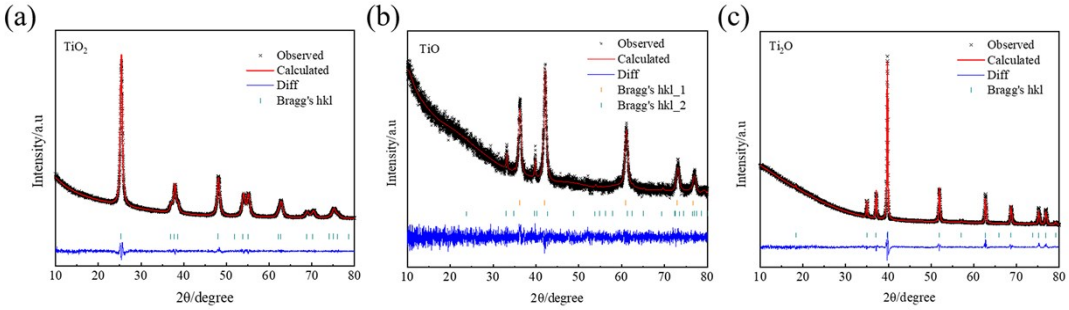

Figure S2 Rietveld refined XRD patterns of (a) raw TiO_2, (b) TiO and (c) Ti_2O

Table S1. Crystallographic data for raw TiO_2, TiO and Ti_2O obtained from the rietveld refined XRD

	Raw TiO_2	TiO		Ti_2O
		TiO phase	Ti_2O_3 phase	
Crystal system	Tetragonal	Cubic	Hexagonal	Hexagonal

Space group	*I41/amd*		*Fm-3m*		*R-3c*		*P-3m1*	
Lattice parameters	*a* (*b*)=3.7870(16), *c* =9.5107(40) (Å), α (β, γ) =90 °		*a* (*b, c*)=4.3955(70) (Å), α (β, γ) =90 °		*a* (*b*)=5.1451(38), *c* =13.6179(96) (Å), α (β) =90 °, γ =120 °		*a* (*b*)=2.960827(93), *c* =4.83708(18) (Å), α (β) =90 °, γ =120 °	
Atom	Ti1	O1	Ti1	O1	Ti1	O1	Ti1	O1
Wyckoff	4a	8e	4a	4b	12c	18e	2d	1a
x	0	0	0	0.5	0	0.3133	0.6667	0
y	0	0	0	0.5	0	0	0.3333	0
z	0	0.20899(13)	0	0.5	0.34485	0.25	0.26515(66)	0
B_{iso} ($Å^2$)	0.151(22)	0.101(46)	0.100(96)	1.50(14)	0.5(2)	0.5(2)	0.100(53)	0.142(17)
Lattice strain	0.15767		0.00003				0.00785	
Average length of Ti-O bond (Å)	1.9512		2.1477		2.0434		2.137	
Cell volume ($Å^3$)	136.39(13)		79.26(39)		312.20(48)		36.7231(27)	
R_{wp}	5.573%		5.838%				4.054%	
R_p	4.293%		4.401%				2.553%	

The small values of R_{wp} and R_p demonstrate that the refined data is reliable.

3. Comparison of Ti 2p XPS spectra of TiO and Ti_2O before and after etching

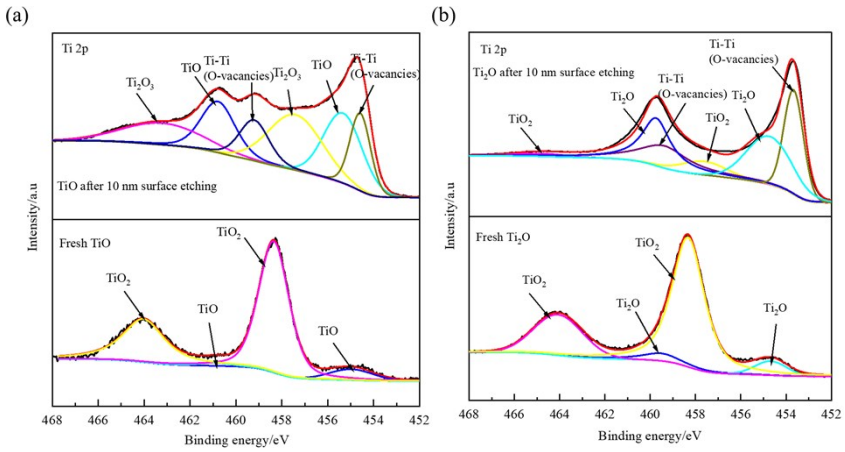

Figure S3 Comparison of Ti 2p XPS spectra of (a) TiO and (b)Ti_2O before and after etching.

As shown in the figure S3b, the high-resolution Ti 2p XPS spectra of Ti_2O sample after 10 nm surface etching can be fitted to six peaks which are located at 453.7 eV, 454.7 eV, 457.6 eV, 459.4 eV, 459.7 eV and 464.9 eV, respectively. The peaks at 454.7 and 459.7 eV corresponds to Ti_2O phase. The peaks around 457.6 eV and 464.9 eV can be attributed to TiO_2 derived from oxidation of Ti_2O in the air. The peaks at 453.7 eV and 459.4 eV can be assigned to Ti-Ti bonds formed by O vacancies in the sublattice.[7] For TiO, six peaks can be fitted in the XPS results of TiO sample after 10 nm surface etching (Figure S3a). The peaks at 455.3 eV and 460.8 eV are ascribed to the TiO phase. The binding energies at 457.4 eV and 463.2 eV can be assigned to Ti_2O_3 phase. The peaks located at 454.3 eV and 459.2 eV are attributed to Ti-Ti bonds originated from the O vacancies in the sublattice. The photoelectron peaks of low-valence titanium oxide are much stronger in the sample with 10 nm surface depth etching, which further proves that there is indeed a layer of TiO_2 oxide film on the surface of TiO and Ti_2O samples.

4. *I-V* curves of raw TiO_2, TiO and Ti_2O

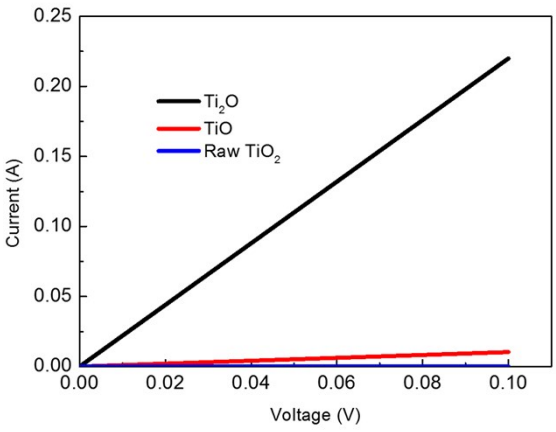

Figure S4 *I-V* curves of raw TiO_2, TiO and Ti_2O.

5. Density function theory (DFT) calculations for raw TiO_2, TiO and Ti_2O

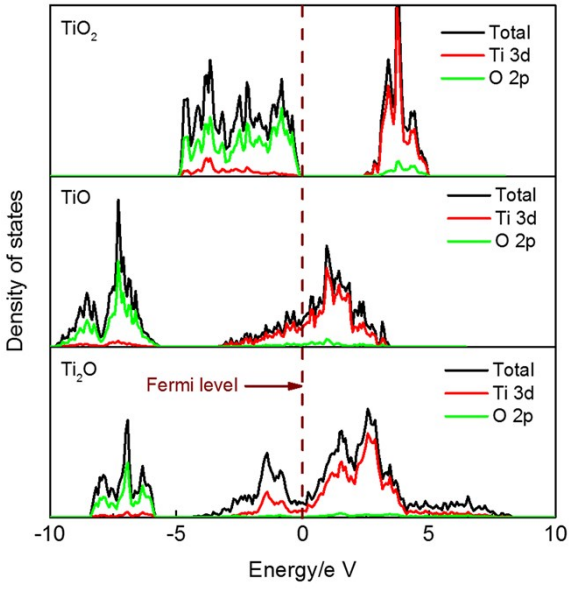

Figure S5 The density of states of raw TiO_2, TiO and Ti_2O. The dotted line represents the Fermi level.

6. CV curves of TiO electrode

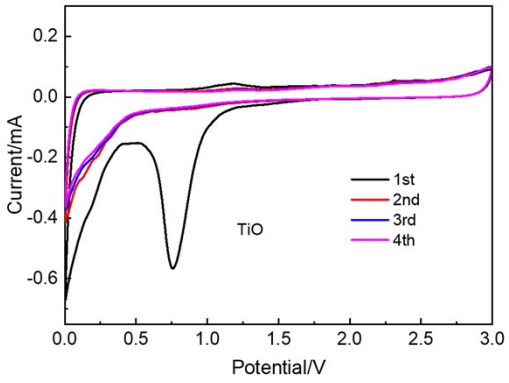

Figure S6 CV curves of TiO electrode at a sweep rate of 0.1 mV s^{-1} between 0.005-3 V (vs Na/Na^+).

7. Charge/discharge curves of TiO electrodes

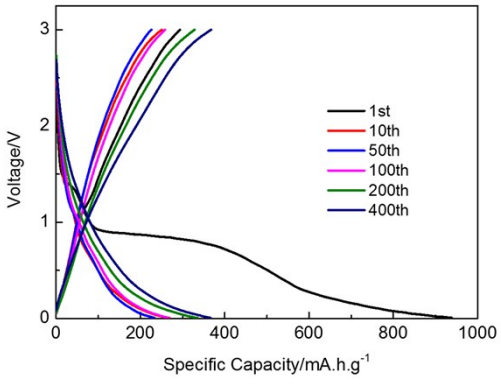

Figure S7 Charge/discharge curves of TiO electrode at a current density of 200 mA g^{-1}.

8. Survey XPS spectra of further washed Ti_2O

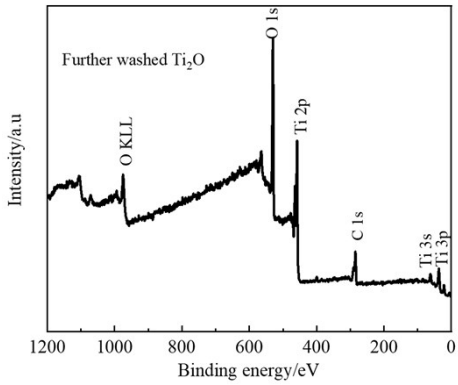

Figure S8 Survey XPS spectra of further washed Ti_2O.

9. SEM, TEM images of further washed Ti_2O and comparison of electrochemical performance of Ti_2O electrode and further washed Ti_2O electrode.

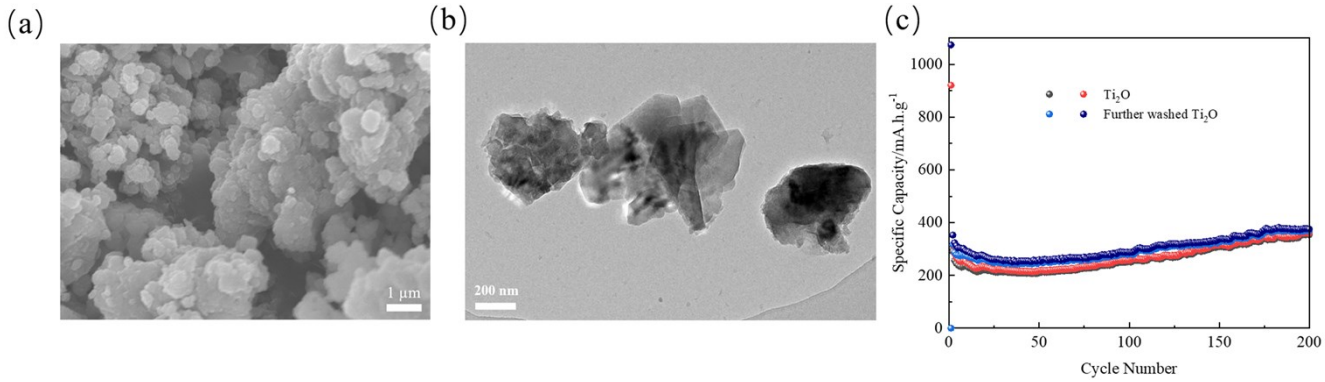

Figure S9 (a) SEM, (b) TEM images of further washed Ti_2O and (c) comparison of electrochemical performance of Ti_2O electrode and further washed Ti_2O electrode.

10. SEM images of Ti_2O electrode after different cycles at fully charged state

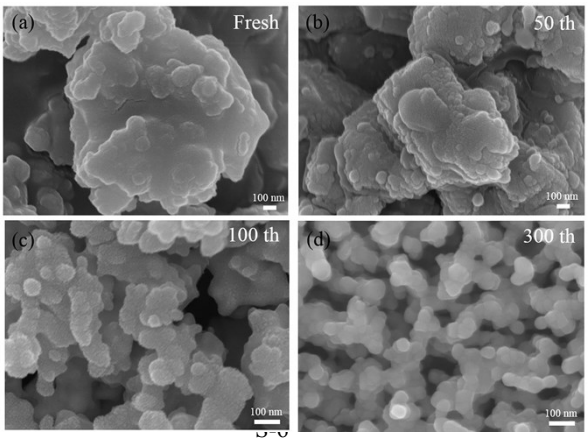

Figure S10 SEM images of Ti_2O electrode after different cycles at fully charged state

11. Ex-situ TEM images of Ti_2O electrode.

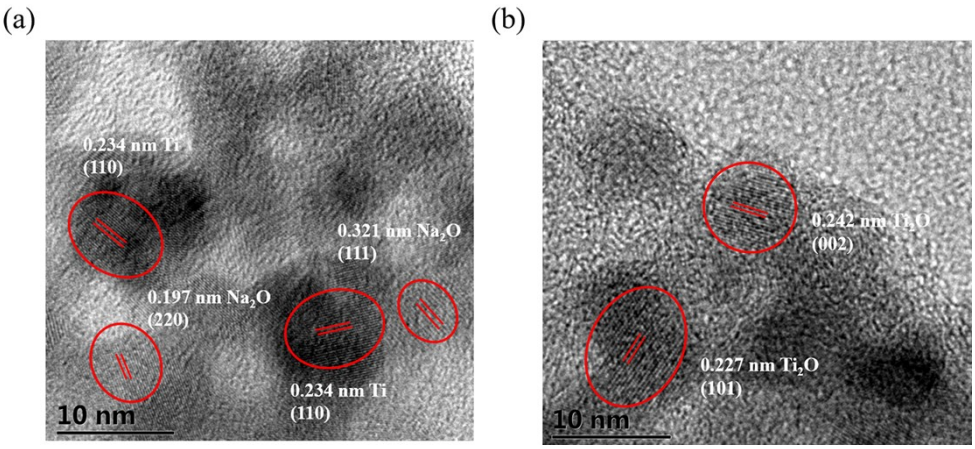

Figure S11 Ex-situ TEM images of Ti_2O electrode at fully discharge and charge states in the first cycle.

As shown in this Figure, when discharged to 0.005 V, the lattice fringes with interplanar distances of 0.234, 0.321 and 0.197 nm are observed in the HRTEM image (Figure S8a), corresponding to (110) crystal planes of Ti and (111), (220) crystal planes of Na_2O, indicating Ti_2O is absolutely reduced to Ti during the full discharge process. Once recharged to 3.0 V, the HRTEM image reveals two clear lattice fringes with spacing of 0.242 and 0.227 nm (Figure S8a), which can be ascribed to the (002) and (101) crystal planes of the Ti_2O, confirming the oxidation of metallic Ti to Ti_2O. The above analysis are agreed well with the results of others ex-situ characterizations.

12. Ex-situ Raman spectra of Ti_2O electrode.

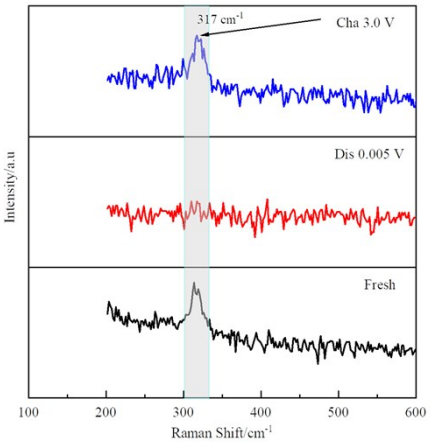

Figure S12 Ex-situ Raman spectra of Ti_2O electrode at fully discharge and charge states in the first cycle.

In this Figure, when discharged to 0.005 V, the disappearance of the vibration characteristic peak of Ti_2O at 317 cm^{-1}, indicating the fracture of Ti-O band during the full discharge process. When fully recharged back

to 3.0 V, the vibration characteristic peak of Ti_2O reappear, suggesting the high electrochemical reversibility of Ti_2O electrode.

13. Ex-situ XRD patterns of Ti_2O electrode at discharge and charge states in the 200th cycle.

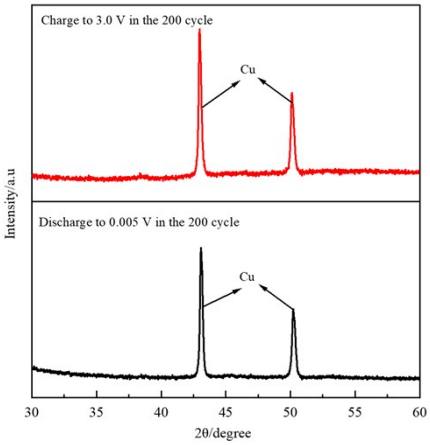

Figure S13 Ex-situ XRD patterns of Ti_2O electrode at discharge and charge states in the 200th cycle.

14. Ex-situ XPS spectra of Ti_2O electrode at discharge and charge states in the 200th cycle.

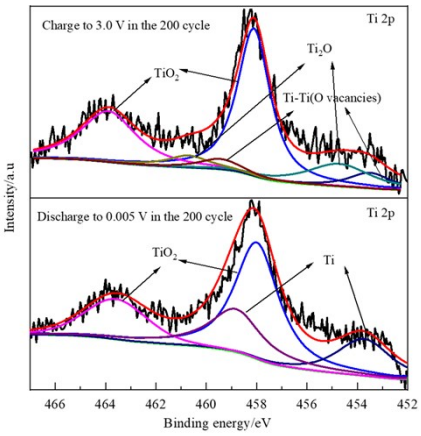

Figure S14 Ex-situ XPS spectra of Ti_2O electrode at discharge and charge states in the 200th cycle.

15. N_2 adsorption–desorption isotherm of the raw TiO_2 and Ti_2O samples.

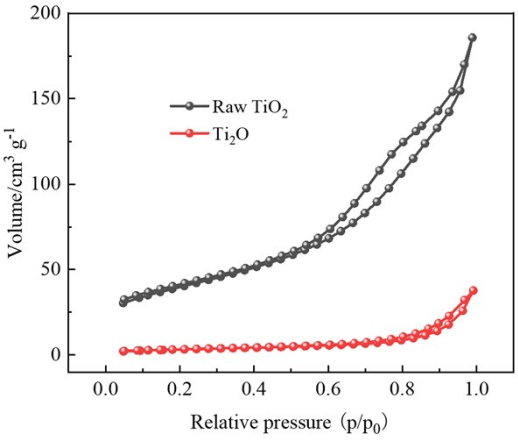

Figure S15 N_2 adsorption–desorption isotherm of the raw TiO_2 and Ti_2O samples.

16. Electrochemical impedance spectra (EIS) and equivalent circuit model of raw TiO_2, TiO and Ti_2O electrodes.

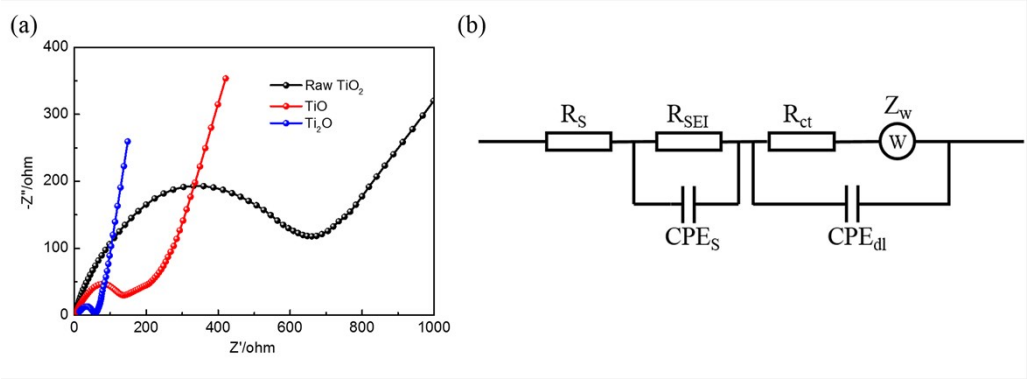

Figure S16 Electrochemical impedance spectra (EIS) and equivalent circuit model of raw TiO_2, TiO and Ti_2O at fully charge state after 100 cycles.

Table S2. Fitting results for the Nyquist plots obtained using the equivalent circuit.

Samples	$R_S(\Omega)$	R_{SEI} (Ω)	CPE_S(F)	$R_{ct}(\Omega)$	CPE_{dl}(F)	Chi-Squared
Raw TiO_2	3.3	46.6	3.7×10^{-6}	533.9	5.4×10^{-7}	1.4×10^{-3}
TiO	4.0	7.3	2.9×10^{-6}	115.9	2.3×10^{-6}	3.1×10^{-3}
Ti_2O	11.5	1.3	1.9×10^{-5}	41.6	2.2×10^{-6}	4.5×10^{-4}

17. D_{Na+} diffusion coefficient calculation.

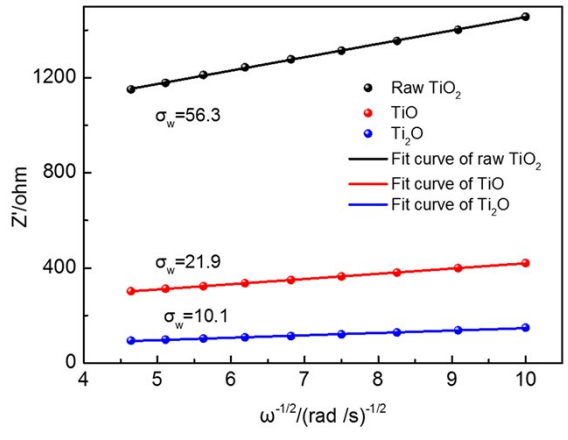

Figure S17 Graph of the inverse square root of angular frequency as a function of Warburg impedance

The solid-state diffusion of sodium ions D_{Na+} through CuS can be estimated by using the following equations:

$$D = \frac{R^2T^2}{2A^2F^4n^4C^2\sigma_W^2} \qquad (S1)$$

$$Z' = R_S + R_{ct} + \sigma_W\omega^{-0.5} \qquad (S2)$$

wherein R is the gas constant, T is the absolute temperature, F is the Faraday constant, A is the footprint area of the electrode, n is the number of electrons involved in the half-reaction for the redox couple, C is the molar concentration of sodium ions in a solid, and σ_w is the Warburg coefficient. R, T, and F are constant. A, n, and C remain consistent in the samples of CuS-b and CuS during tests. Figure 4f shows that the σ_w of raw TiO_2, TiO and Ti_2O are 56.3, 21.9 and 10.1 ($\Omega\ s^{-1/2}$), respectively. Thus, low-valence titanium oxides have larger D_{Na+} than raw TiO_2.

18. XRD pattern of $Na_3V_2(PO_4)_3/C$.

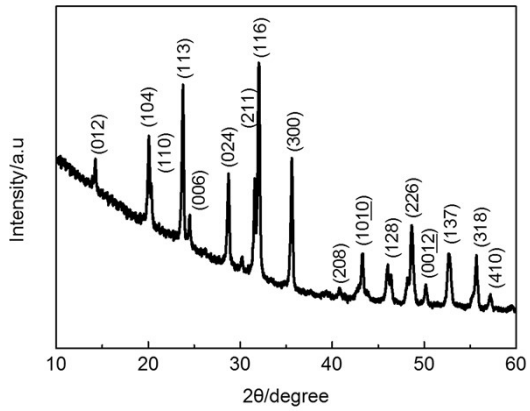

Figure S18 XRD pattern of $Na_3V_2(PO_4)_3/C$

19. TG curve of $Na_3V_2(PO_4)_3/C$.

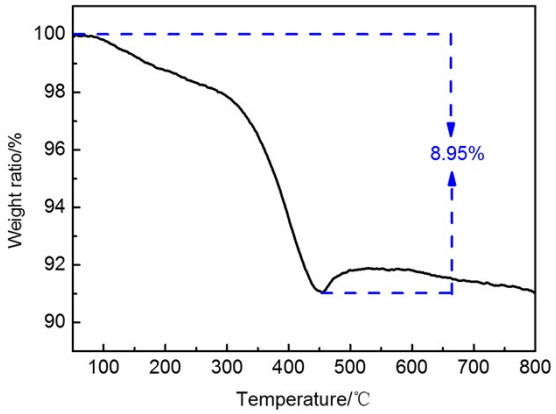

Figure S19 TG curve of $Na_3V_2(PO_4)_3$/C

20. SEM image of $Na_3V_2(PO_4)_3$/C.

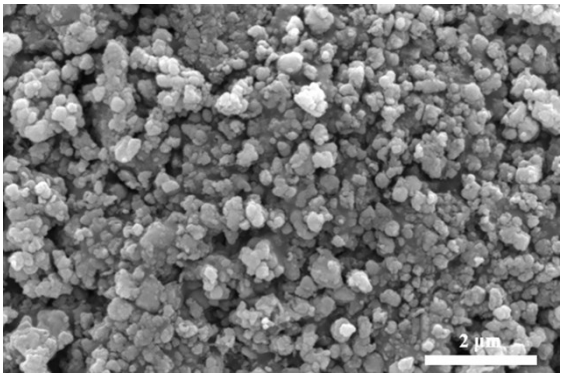

Figure S20 SEM image of $Na_3V_2(PO_4)_3$/C

21. electrochemical performance of $Na_3V_2(PO_4)_3$/C cathode.

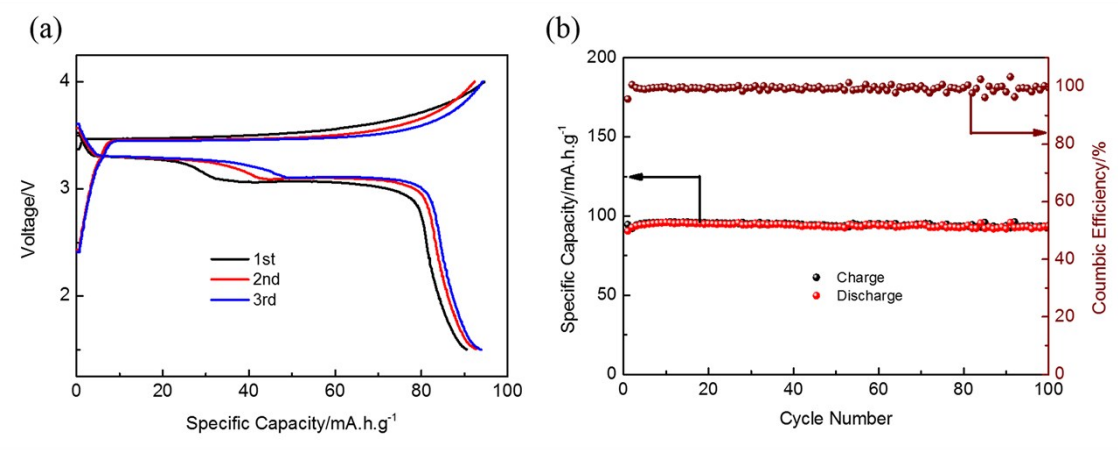

Figure S21 (a) charge/discharge profiles of $Na_3V_2(PO_4)_3$/C electrode in the initial three cycles, (b) cycling performance of $Na_3V_2(PO_4)_3$/C electrode at a current density of 200 mA g^{-1}.

References

1. G. Kresse and J. Furthmüller, *Comp.mat.er*, 1996, **6**, 15-50.
2. G. Kresse and F. J, *Phys. Rev. B*, 1996, **54**, 11169-11186.
3. J. P. Perdew, K. Burke and M. Ernzerhof, *Phys. Rev. Lett.*, 1996, **77**, 3865--3868.
4. G. Kresse and D. Joubert, *Phys. Rev. B*, 1999, **59**, 1758-1775.
5. P. E. Blochl, *Phys. Rev. B Condens Matter*, 1994, **50**, 17953-17979.
6. S. L. Dudarev, G. A. Botton, S. Y. Savrasov, C. J. Humphreys and A. P. Sutton, *Phys. Rev. B*, 1998, **57**, 1505-1509

7. A. Singh and V. Kalra, *ACS Appl. Mater. Interfaces*, 2018, **10**, 37937-37947.